Energy Conversion and Management 284 (2023) 116982

Contents lists available at ScienceDirect

Energy Conversion and Management

journal homepage: www.elsevier.com/locate/enconman

Optimal electrode coverage based on a new criterion for piezoelectric energy harvesters

Lan Shang [a,b], Christophe Hoareau [c], Andreas Zilian [a,*]

[a] Department of Engineering, University of Luxembourg, Luxembourg
[b] Research Center for Intelligent Computing Platforms, Zhejiang Lab, China
[c] Laboratoire de Mécanique des Structures et des Systèmes Couplés (LMSSC), Conservatoire national des arts et métiers (Cnam), France

ARTICLE INFO

Keywords:
Piezoelectric energy harvesting
Electrode coverage optimization
Design criterion
Beam cross-section rotation

ABSTRACT

Piezoelectric energy harvesters (PEHs) are a promising alternative to conventional electrochemical batteries with the advantage of being self-powered and maintenance-free, but their application is severely restricted by the low electric power output. It has been reported that the power output of PEHs can be enhanced by well-designed electrode coverage. A common design criterion for beam-like PEHs is based on the strain node to avoid electrode charge cancellation. This criterion, however, is not feasible for PEHs subject to complex spatio-temporal excitation patterns, where strain nodes change their position. This work proposes a new design criterion for optimal electrode coverage of beam-like PEHs based on the closed-form solution of the circuit equation that expresses voltage as a function of the beam's dynamic response, specifically the cross-section rotation. The new criterion maximizes the averaged curvature of the beam segment covered by the electrode using data on the instantaneous rotation field. The improved physical significance and reliability of the presented criterion are discussed. The associated electrode optimization procedure is then exemplified for PEHs driven by fluid flow, which helps to realize a complex excitation pattern. Two numerical studies, both including a variety of combinations of fluid densities and inlet velocities, are performed to demonstrate that an optimal electrode configuration can be obtained with the proposed criterion. Comparison of different electrode configurations in above studies finally leads to useful conclusions on the power output and electrode configuration.

1. Introduction

The conversion of electric energy from mechanical energy existing naturally in surroundings via piezoelectric energy harvesters (PEHs) is an emerging technique to implement sustainable power supply at reduced maintenance cost [1]. As a self-powered energy source, PEHs are in particular promising in applications where it is infeasible to recharge or replace conventional electrochemical batteries, e.g., large-scale wireless sensor networks. A prevalent concern in PEHs is the low power output, which, nevertheless, could be mitigated by several ways, including but not limited to: enhanced materials [2], elaborate geometry for piezoelectric structures [3,4], power conditioning circuits [5], and proper disposal of electrodes [6,7]. The last one is the topic of this work.

Although electrodes normally have inconsequential influence on the mechanical behavior of PEHs, their configuration greatly affects the power output due to the fact that they play a critical role in the energy conversion. More specifically, if applying an external force to deform a piezoelectric material (i.e., input mechanical energy), the material will be polarized [8], inducing an electric field; if the material is covered by electrodes and further connected with a circuit, free charges in the electrodes will be driven by the electric field to flow through the circuit to generate an electric current (i.e., output electric energy). The free charges contributing to the electric current are highly relevant to the bending strain distribution of the piezoelectric material over the electrode area [9].

For a beam-like PEH subject to vibration, the bending strain in the piezoelectric layer is very likely not uniform or even changes its sign in the longitudinal direction. The sign denotes if the strain is compression or extension, and the axial position where the change occurs is called the strain node. For example, given a cantilevered beam, which is the extensively investigated structure for PEHs, when it is vibrating at the first mode (Fig. 1(a)), the bending strain is larger near the clamped root while zero at the free end, yet with the same sign; when it is vibrating

* Corresponding author.
E-mail addresses: shanglan@zhejianglab.com (L. Shang), christophe.hoareau@lecnam.net (C. Hoareau), andreas.zilian@uni.lu (A. Zilian).

https://doi.org/10.1016/j.enconman.2023.116982
Received 9 December 2022; Received in revised form 23 March 2023; Accepted 27 March 2023
Available online 4 April 2023

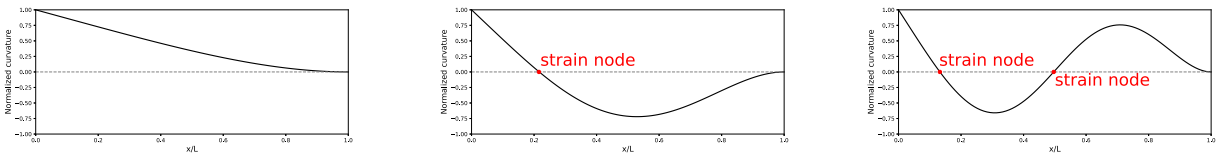

(a) First vibration mode (b) Second vibration mode (c) Third vibration mode

Fig. 1. Normalized curvature (bending strain) of a cantilevered Euler–Bernoulli beam for the first three vibration modes.

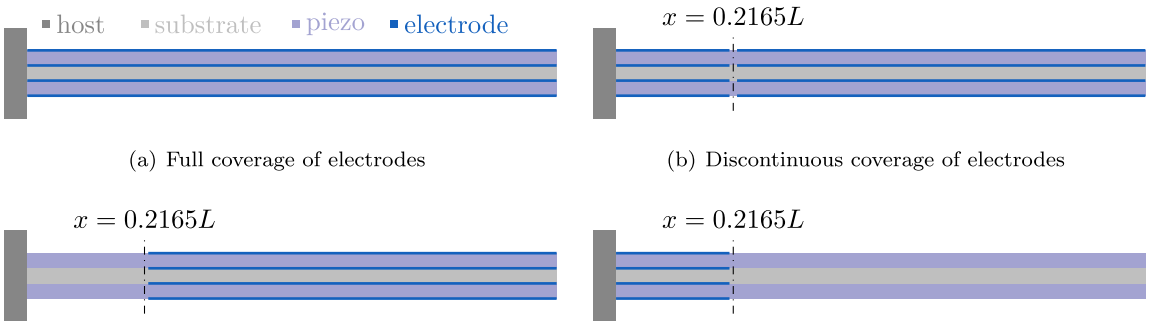

(a) Full coverage of electrodes (b) Discontinuous coverage of electrodes

(c) Partial coverage of electrodes from the free end (d) Partial coverage of electrodes from the clamped root

Fig. 2. Different electrode configurations. The last three figures, which take a PEH vibrating in the second mode as an example, illustrate the methods in literature to avoid charge cancellation.

at other modes (Figs. 1(b)–1(c)), the bending strain is not only uneven but also with different sign.

If the strain is uneven, the free charges need to redistribute to satisfy the equipotential condition over the electrode area, inducing energy dissipation [10,11]. This energy dissipation could not be compensated by increasing the electrode area, so full electrode coverage (Fig. 2(a)), which means the two surfaces along the beam length direction of the piezoelectric layer are completely covered by a pair of continuous electrodes, is not always the optimal electrode configuration to harvest the most energy. If the strain changes the sign, full coverage may cause more severe energy loss because of charge cancellation [9]. To avoid charge cancellation, effective methods are to use discontinuous electrodes which break at the strain node(s) [9,12,13] (multiple pairs of electrodes, Fig. 2(b)), or to cover only partially the beam surfaces with electrodes from the clamped root or the free end to the strain node [14] (a single pair of electrodes, Figs. 2(c)–2(d)).

The methods mentioned above [9,12–14] can be seen as strain node based methods since they at first identify the strain node, and then try to not cover the strain node. They are popular in literature, especially for PEHs operating under base excitation with a specific (higher than 1st) modal frequency, in which situation the strain node has a fixed location on the beam and can be easily identified by modal analysis. No coverage of the strain node can definitely improve the voltage output when compared with the electrode configuration of full coverage because charge cancellation is avoided, but it lacks sufficient consideration for energy dissipation induced by uneven strain. In addition, when it comes to PEHs undergoing complex vibration, e.g., flow-driven PEHs operating under limit cycle oscillations (LCOs), there is no fixed location for the strain node. In such cases, apparently strain node based methods would not be feasible. Paper [14] investigates a flow-driven PEH. It indicates that the strain node is mostly placed in a specific region under a given flow regime, and finally the position in an average sense is regarded as the strain node by [14].

This work proposes a new criterion for partial coverage of electrodes to improve the power output of beam-like PEHs. The new criterion does not need the identification of strain nodes, so it can be easily applied not only to base-excited PEHs, but also to flow-driven PEHs, which are the focus of this work. The new criterion takes into account the effect of energy dissipation induced by uneven strain, so it can achieve higher voltage output than that of strain node based methods.

The remainder of this work is organized as follows. Section 2 introduces the governing equations for the multiphysics system of a flow-driven PEH. Section 3 proposes the new criterion, which is based on an explicit expression of the voltage with respect to (w.r.t.) the beam cross-section rotation. Section 4 demonstrates through two numerical studies that optimal design of electrode configuration for a flow-driven PEH can be obtained using the new criterion. Interesting phenomena shown in the two studies are also discussed. Section 5 analyses the strengths and weaknesses of the new criterion. Finally, Section 6 summarizes the contributions of this article.

2. Governing equations of a flow-driven PEH

The two-dimensional schematic illustration of a flow-driven PEH is shown in Fig. 3. The PEH consists of a piezoelectric laminate (layers stacked in the beam thickness direction z) and an electric circuit with a resistive load and electrodes, and it is straight initially, surrounded by an axial flow (fluid flows in the beam length direction x). When the fluid velocity exceeds a critical value, the cantilevered structure will undergo self-induced, self-sustained vibration with a constant amplitude, i.e., limit cycle oscillations, which are a flutter phenomenon resulting from structural and/or fluid non-linearity [15]. We assume that the electrodes fully cover the surfaces of piezoelectric layers in the beam width direction, but may not in the beam length direction. There are two common cases of partial coverage of electrodes, distinguished from each other by whether the length of piezoelectric layers varies according to that of electrodes. If so, changing the length of electrodes means the geometrical parameter of the laminate structure changes as well, which might cause significant influence on the structural dynamics. If not, i.e., if the piezoelectric layers are always as long as the substrate layer, changing the length of electrodes will have negligible influence on the structural dynamics. This work considers the latter case.

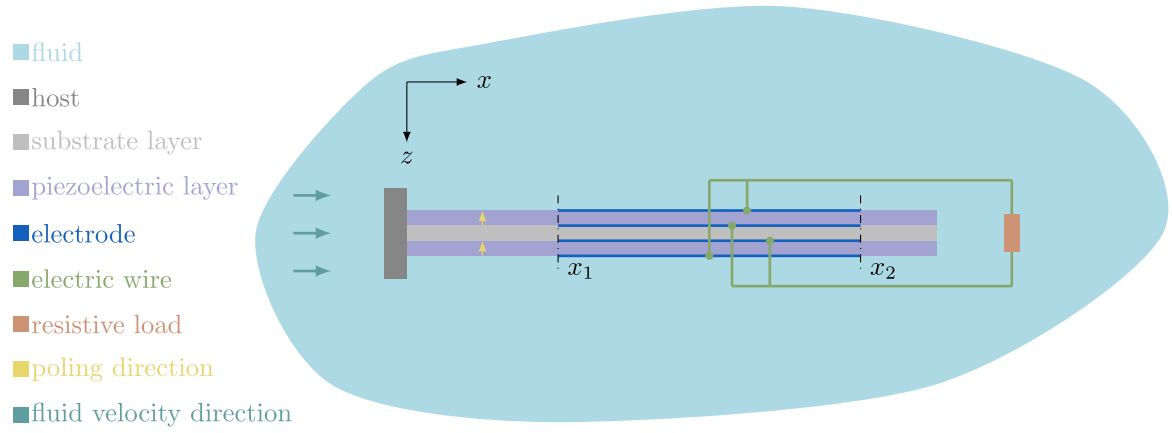

Fig. 3. A PEH consisting of a piezoelectric laminate and an electric circuit immersed in a fluid flow.

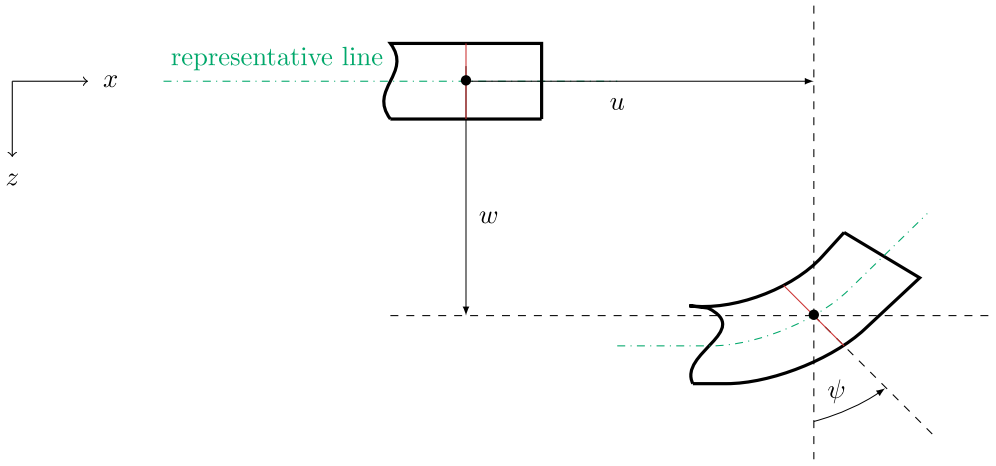

Fig. 4. Planar beam with large displacement/rotation and first-order shear deformation.

2.1. Structure

The piezoelectric laminate is modeled using the geometrically exact beam theory [16], which allows for large displacement/rotation and first-order shear deformation of the structure in the $x-z$ plane, as shown in Fig. 4. With appropriate coupling conditions enforced between layers, the structural dynamics of the laminate can be described by the motion of a representative line [17]. Following this way, the momentum balance equation for the laminate subject to the fluid force reads

$$\mathbf{M}\frac{\partial^2 \mathbf{d}}{\partial t^2} - \mathfrak{R}(\mathbf{d}) - \mathbf{f} = \mathbf{0}, \tag{1}$$

where t is time, $\mathbf{M}$ is a matrix composed of the inertial parameters of the laminate, $\mathbf{d}$ is a vector collecting axial displacement u, transverse displacement w and beam cross-section rotation ψ, $\mathfrak{R}(\mathbf{d})$ is a term indicating the elastic behavior of the laminate, and $\mathbf{f}$ is the external fluid force. For the sake of brevity, the details of Eq. (1) are not provided. Additionally, piezoelectricity is accounted for in the structural model by introducing the linear constitutive laws of piezoelectric materials. The constitutive laws finally result in one term of the electric potential energy in piezoelectric layers, and another term of the electromechanical coupling. Both terms are related to the voltage output. For further information of Eq. (1) and the two terms, readers could refer to [17], which focuses on the modeling of PEHs.

2.2. Fluid

The Navier–Stokes equations are adopted to represent the dynamics of the incompressible, viscous fluid surrounding the PEH, expressed as

$$\rho\left(\frac{\partial \mathbf{v}}{\partial t} + \mathbf{v}\cdot\nabla\mathbf{v}\right) - \nabla\cdot\mathbf{T} = \mathbf{0}, \tag{2}$$

$$\nabla\cdot\mathbf{v} = 0, \tag{3}$$

where $\rho, \mathbf{v}, \mathbf{T}$ are density, velocity and Cauchy stress tensor of the fluid, respectively. The constitutive relation is given by

$$\mathbf{T} - \mu(\nabla\mathbf{v} + (\nabla\mathbf{v})^{\mathrm{T}}) + p\mathbf{I} = \mathbf{0}, \tag{4}$$

where μ is dynamic viscosity, p is hydrostatic pressure, and $\mathbf{I}$ is an identity tensor.

2.3. Electric circuit

The electric circuit attached to the piezoelectric laminate is modeled according to Ohm's law and Gauss' law, given by [18]

$$\frac{\mathrm{d}}{\mathrm{d}t}\left(\int_A \mathbf{D}\cdot\mathbf{n}\mathrm{d}A\right) = \frac{\phi}{R}, \tag{5}$$

where $\mathbf{D}$ is the electric displacement in piezoelectric layers, $\mathbf{n}$ is the unit outward normal, A is the electrode area, R is the resistive load, and ϕ is the voltage output. ϕ is only temporally dependent due to the equipotential condition, thus denoted as $\phi(t)$ when necessary.

In this work, we consider a bimorph with a parallelly connected circuit, as shown in Fig. 3. Assuming linear constitutive laws and uniform

electric field across the thickness of the piezoelectric layer [17,18], when the electrode covers the piezoelectric layer from x_1 to x_2, the left hand side of Eq. (5) can be calculated using the geometrical and material parameters of the PEH, leading to

$$-e_{31}b(h_S+h_P)\frac{d\psi(x,t)|_{x_1}^{x_2}}{dt}-\frac{2b\epsilon_{33}^S(x_2-x_1)}{h_P}\frac{d\phi(t)}{dt}=\frac{\phi(t)}{R}, \tag{6}$$

where e_{31} is the piezoelectric constant, ϵ_{33}^S is the permittivity component at constant strain, and h_S, h_P, b are the thickness of the substrate layer, thickness of the piezoelectric layer and the width of the laminate, respectively. Eq. (6) is not common in literature since most relevant papers are based on the Euler–Bernoulli beam assumptions, hence the beam cross-section rotation is not explicitly present in the circuit equation. Paper [19] has an equation similar to Eq. (6), but it deals with PEHs fully covered by electrodes. The detailed derivation of Eq. (6) can be found easily in literature, e.g., in the aforementioned paper [19], changing the integral interval from $[0, L]$ (L is the beam length) for full coverage to $[x_1, x_2]$ for partial coverage; or in paper [12], with an adaption from the Euler–Bernoulli beam assumptions to the Timoshenko beam assumptions.

2.4. Solution scheme

To figure out the fluid force **f** acting on the PEH, or in other words, to solve the fluid–structure interaction (FSI) problem governed by Eqs. (1)–(4), particular efforts are needed on the numerical solution scheme. Our previous work [20] is aimed at this. In brief, the FSI problem (including the two terms mentioned in Section 2.1 and the circuit Eq. (5)) is solved in a monolithic fashion with the boundary-fitted finite element method (FEM) used for the discretization in space, and the generalized-α method for discretization in time.

3. A new criterion to optimize electrode coverage: averaged curvature criterion

3.1. Expression of voltage with respect to beam cross-section rotation

For a PEH bearing a given resistive load R, the power output is ϕ^2/R, so the key to the prediction of power output is the prediction of voltage ϕ. Although for the flow-driven PEH, ϕ is obtained by means of a particular numerical solution scheme as mentioned in Section 2.4, an approximate expression of ϕ derived through an analytic method is still possible. The voltage is directly related to the structural dynamics only, implying that ϕ can be determined once the dynamic response of the structure is known. Furthermore, considering the physical significance of the two terms omitted in Eq. (1), i.e., one for the electric potential energy, and one for the electromechanical coupling, it is reasonable not to take them into account when estimating the voltage. As a consequence, Eq. (6) alone is enough to determine the relation between the voltage and structural dynamics.

Eq. (6) can be regarded as a first order linear differential equation of the unknown $\phi(t)$. Accordingly, the solution[1] is

$$\phi(t)=e^{-\int\frac{h_P}{2Rb\epsilon_{33}^S(x_2-x_1)}dt}\left(\int e^{\int\frac{h_P}{2Rb\epsilon_{33}^S(x_2-x_1)}dt}\left(-\frac{e_{31}h_P(h_S+h_P)}{2\epsilon_{33}^S(x_2-x_1)}\times\frac{d\psi(x,t)|_{x_1}^{x_2}}{dt}\right)dt+C\right), \tag{7}$$

where C is a constant of integration. After integration by parts, Eq. (7) can be written as

$$\phi(t)=+Ce^{-\int\frac{h_P}{2Rb\epsilon_{33}^S(x_2-x_1)}dt} \tag{8-1}$$

$$-\frac{e_{31}h_P(h_S+h_P)}{2\epsilon_{33}^S}\frac{\psi(x,t)|_{x_1}^{x_2}}{x_2-x_1} \tag{8-2}$$

$$-e^{-\int\frac{h_P}{2Rb\epsilon_{33}^S(x_2-x_1)}dt}\left(\int\frac{de^{\int\frac{h_P}{2Rb\epsilon_{33}^S(x_2-x_1)}dt}}{dt}\left(-\frac{e_{31}h_P(h_S+h_P)}{2\epsilon_{33}^S}\times\frac{\psi(x,t)|_{x_1}^{x_2}}{x_2-x_1}\right)dt\right). \tag{8-3}$$

Provided that when $t=0$, there is no structural deformation, and thus no voltage output, i.e., $\phi(t=0)=0$, $\psi(x,t=0)=0$, C can be inferred to be zero from Eq. (8). Therefore, the expression of voltage $\phi(t)$ w.r.t. beam cross-section rotation $\psi(x,t)$ is finally given by Eqs. (8-2) and (8-3). We note that $\psi(x,t)$ is present with the boundary of integration x_1, x_2, so the voltage $\phi(t)$ represented by Eq. (8) is still spatially independent (not being a function of x), which is consistent with the equipotential condition.

3.2. Averaged curvature criterion (ACC)

Eq. (8) cannot be used to compute $\phi(t)$ without knowing $\psi(x,t)$, but it provides a clue to optimize the electrode configuration. There is a multiplier shared by both Eqs. (8-2) and (8-3), i.e., $\frac{\psi(x,t)|_{x_1}^{x_2}}{x_2-x_1}$, which is directly associated with the electrode placement. Inspired by this, we postulate that the change of $\phi(t)$ w.r.t. x_1, x_2 (not x) may largely share the same trend as the change of $\frac{\psi(x,t)|_{x_1}^{x_2}}{x_2-x_1}$ w.r.t. x_1, x_2. This implies that $\frac{\psi(x,t)|_{x_1}^{x_2}}{x_2-x_1}$ can be taken as a simple intermediate indicator to represent the change (not the value) of $\phi(t)$. Therefore, a good choice of electrode locations x_1, x_2 to improve voltage output $\phi(t)$ could be identified from beam cross-section rotation $\psi(x,t)$ by improving $\frac{\psi(x,t)|_{x_1}^{x_2}}{x_2-x_1}$. Obviously, an extreme inference from the above postulation is that the maximum (absolute) value of $\frac{\psi(x,t)|_{x_1}^{x_2}}{x_2-x_1}$ corresponds to the maximum (absolute) value of $\phi(t)$.

By definition, the beam curvature κ is $\kappa(x,t)=\frac{\partial\psi(x,t)}{\partial x}=\lim_{\Delta x\to 0}\frac{\psi(x+\Delta x,t)-\psi(x,t)}{\Delta x}$, so it makes sense to regard $\frac{\psi(x,t)|_{x_1}^{x_2}}{x_2-x_1}$ as the averaged curvature of the electrode covered beam. Thus we call the method of electrode optimization by maximizing the intermediate indicator $\frac{\psi(x,t)|_{x_1}^{x_2}}{x_2-x_1}$ as the averaged curvature criterion, ACC in short.

3.3. Physical significance of ACC

The numerator of $\frac{\psi(x,t)|_{x_1}^{x_2}}{x_2-x_1}$ is the integral of the curvature (bending strain) over the electrode length $[x_1, x_2]$, so it can be seen as an indicator of the effect of the strain node (or the sign of the bending strain), in the sense that if the sign does not change, the (absolute) value of the integral will be larger when the electrode is longer. The denominator means the integral is averaged over the electrode length, so it can be understood to indicate a quantity is re-distributed to achieve a uniform state. From this perspective, although being simple, ACC incorporates two kinds of physical mechanism, i.e., charge cancellation and charge re-distribution, which are explained in Introduction.

3.4. Preliminary validation of ACC for a base-excited PEH

To examine the validity of ACC, a comparison using the problem setup (Fig. 5) and experimental data presented in [12] is performed. When the PEH operates in the first three vibration modes, the peak

[1] Given a first order linear differential equation of the unknown $y(t)$: $\frac{dy(t)}{dt}+p(t)y(t)=f(t)$, the general solution can be written as $y(t)=e^{-\int p(t)dt}\left(\int e^{\int p(t)dt}f(t)dt+C\right)$.

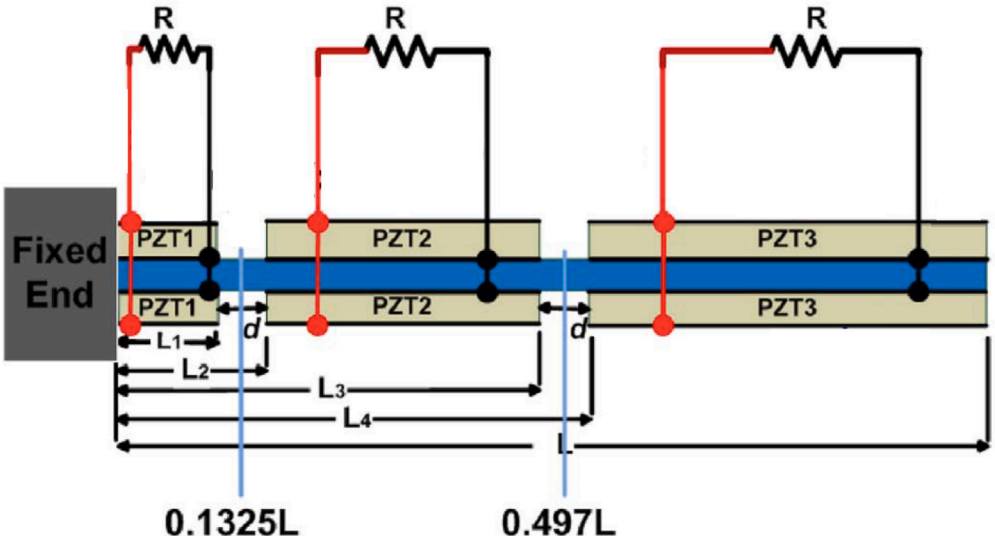

Fig. 5. A cantilevered PEH with three pairs of segmented electrodes, adapted from paper [12] with permission. The full length L is 37 mm, while the length of PZT1, PZT2, PZT3 is 4.8 mm, 13.3 mm, 18.5 mm, respectively. The gap d is 0.2 mm. The positions of the two gaps $0.1325L, 0.497L$ are the two strain nodes for the third vibration mode.

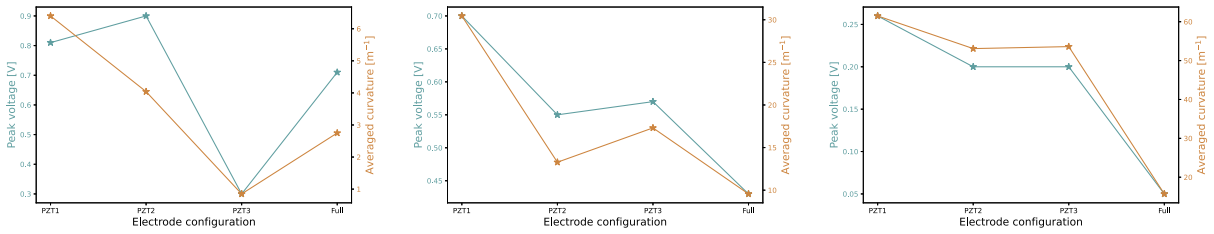

(a) Mode 1 (b) Mode 2 (c) Mode 3

Fig. 6. The sequence of the averaged curvature agrees well with the sequence of the peak voltage.

Table 1
Peak voltage and averaged curvature of a cantilevered PEH with segmented electrodes.

Mode	Peak voltage [V] [12]				Averaged curvature [m^{-1}]			
	PZT1	PZT2	PZT3	Full	PZT1	PZT2	PZT3	Full
1	0.81	0.9	0.3	0.71	6.40	4.04	0.85	2.75
2	0.7	0.55	0.57	0.43	30.45	13.28	17.31	9.56
3	0.26	0.2	0.2	0.05	61.49	53.09	53.60	15.70

voltage available from Table 2 of [12], and the averaged curvature[2] are given in Table 1. Fig. 6 visualizes the data in Table 1. It can be seen from Fig. 6 that the sequence of the averaged curvature agrees well with the sequence of the peak voltage, with only two exceptional cases (underlined by green in Table 1), i.e., PZT1 and PZT2 in the first vibration mode, out of the twelve ($= 3 \times 4$) cases. This comparison shows that ACC is largely reliable, but since $\frac{\psi(x,t)|_{x_1}^{x_2}}{x_2 - x_1}$ does not contain all information of the voltage expression Eq. (8), this criterion might not offer correct indication in some cases. Nevertheless, ACC is simple, thus the optimization of electrode coverage with ACC being much easier than that with the complete form of Eq. (8), so ACC is valuable in practice.

3.5. Comparison of ACC with strain node based methods

The data in Table 1 also provide a good example to exhibit the superiority of ACC over strain node based methods. The latter essentially seeks to maximize the difference of the beam cross-section rotation between the two ends of the electrode, i.e., to maximize $\psi(x,t)|_{x_1}^{x_2} = \psi(x_2,t) - \psi(x_1,t)$. When the PEH is in the first vibration mode (the left of Fig. 7), the maximum (absolute) rotation difference is reached at $x_1 = 0, x_2 = L$, i.e., the electrode fully covering the beam. When in the third vibration mode (the right of Fig. 7), it is reached at $x_1 = 0.4965L, x_2 = L$, i.e., the case of PZT3 in Fig. 5. Observing the first and third rows of voltage data in Table 1, we find that neither of the above two (underlined by red in Table 1) helps to achieve the maximum voltage in the four cases (PZT1, PZT2, PZT3, and full coverage). By contrast, for the third vibration mode, ACC predicts PZT1 (61.49 in Table 1 is the maximum ACC value for mode three) to be the optimal electrode in the four cases, which is true if observing the data of peak voltage in Table 1; for the first vibration mode, ACC predicts PZT1 to be the optimal case, which is not true, but PZT1 is better than the case of full coverage. The data in Table 1 are not relevant for the strain node in the second vibration mode ($x = 0.2165L$), so no comparison of the second mode is presented here.

Remark. Strain nodes locate at the position where the beam curvature is zero, i.e, where $\kappa = \frac{\partial \psi(x,t)}{\partial x} = 0$, so if a short electrode passes through

[2] The modal displacement of a cantilevered Euler–Bernoulli beam is $\bar{w}(\bar{x}) = \cosh(\lambda\bar{x}) - \cos(\lambda\bar{x}) - \frac{\sinh(\lambda)-\sin(\lambda)}{\cosh(\lambda)+\cos(\lambda)}(\sinh(\lambda\bar{x}) - \sin(\lambda\bar{x}))$, where $\bar{x} = x/L$ is the dimensionless x coordinate, and $\lambda = 1.875104, 4.694091, 7.854757$ for the first three vibration modes, respectively. The averaged curvature $|\frac{\psi(x,t)|_{x_1}^{x_2}}{x_2 - x_1}|$ is then computed as $|\frac{\bar{w}'(\bar{x}_2) - \bar{w}'(\bar{x}_1)}{\bar{x}_2 - \bar{x}_1}|$.

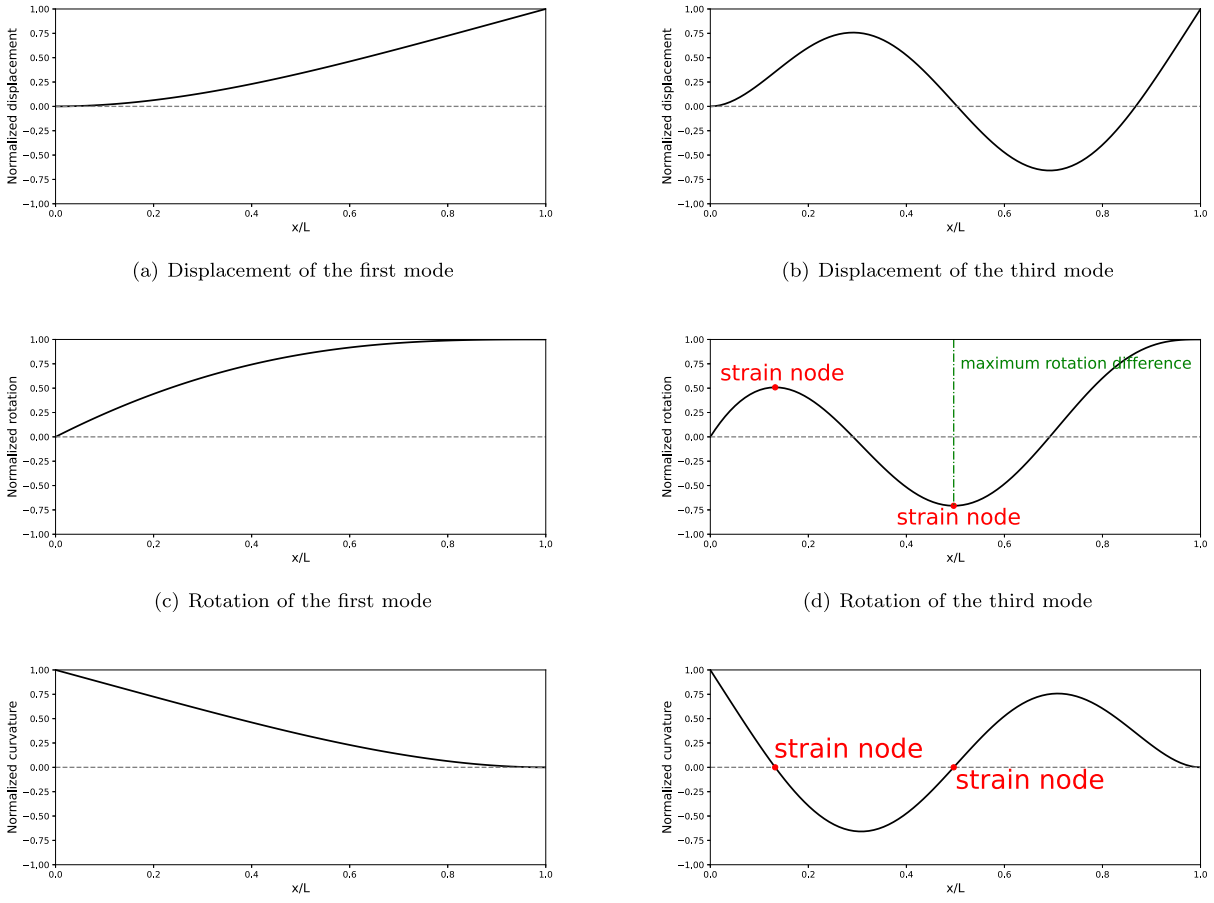

(a) Displacement of the first mode

(b) Displacement of the third mode

(c) Rotation of the first mode

(d) Rotation of the third mode

(e) Curvature of the first mode

(f) Curvature of the third mode

Fig. 7. Normalized displacement, rotation and curvature of a cantilevered beam in the first (left) and third (right) vibration mode.

a strain node, the averaged curvature $\frac{\psi(x,t)|_{x_1}^{x_2}}{x_2-x_1}$ will be close to zero. Since the term $\frac{\psi(x,t)|_{x_1}^{x_2}}{x_2-x_1}$ is present in the voltage expression Eq. (8) (including both Eqs. (8-2) and (8-3)) as a multiplier, the output voltage will be naturally small. This could be an analytical interpretation for the voltage fall-off when the electrode covers a strain node. That also means that the strain node based methods can be taken as a special application of ACC.

4. Optimal electrode coverage based on ACC for a flow-driven PEH

This section is to validate ACC for a flow-driven PEH, i.e., whether a favorable electrode placement to achieve optimal voltage output can be determined with ACC. Denoting the maximum value of output voltage $\phi(t)$ during LCOs with an electrode coverage range $[x_1, x_2]$ under a given fluid condition as $\phi_{\text{peak}}(x_1, x_2)$, the optimization problem is stated as

$$\begin{aligned} &\text{maximize} \quad \phi_{\text{peak}}(x_1, x_2) \\ &\text{subject to:} \quad 0 \le x_1 < x_2 \le L. \end{aligned} \tag{9}$$

The basic idea of the validation, illustrated by Fig. 8, is to compare the output voltage for a series of ranges $[x_1, x_2]$, in which one range is determined based on ACC, i.e., to figure out x_1, x_2 by maximizing $\frac{\psi(x,t)|_{x_1}^{x_2}}{x_2-x_1}$. This is feasible because a discrete (in space and time) dataset of $\psi(x,t)$ can be obtained by numerically solving the theoretical model, as mentioned in Section 2.4. Considering that the electrode configuration has negligible influence on the mechanical response of the PEH structure, the electrode configuration of full coverage is used when collecting the dataset of $\psi(x,t)$.

4.1. Setup of a flow-driven PEH

We consider the flow-driven PEH proposed by [20], which is adapted from a setup in paper [21]. As depicted in Fig. 9, a thin-walled bimorph clamped at point C (0.12, 0.3) is immersed in a uniform axial flow. LCOs of the cantilevered structure can be excited by an initial perturbation if fluid conditions are properly prescribed.

The bimorph length is 5.8×10^{-1} m, the total thickness is 5×10^{-4} m, with $h_{\text{P}} = 1 \times 10^{-4}$ m, $h_{\text{S}} = 3 \times 10^{-4}$ m, and two-dimensional FSI is considered, so width is 1 m. The substrate layer is made from aluminum alloy, of which the density, Young's modulus and Poisson's ratio are 2800 kg m^{-3}, 7×10^{10} Pa, 0.35, respectively. The piezoelectric layers are made from PZT-5A, and the three material parameters are 7800 kg m^{-3}, 6.6×10^{10} Pa, 0.35; in addition, the piezoelectric parameters are $e_{31} = -12.54$ C m^{-2}, $\epsilon_{33}^{S} = 1.3281 \times 10^{-8}$ F m^{-1}. The resistive load in the circuit is $R = 50$ kΩ. For the fluid, the dynamic viscosity is $\mu = 0.2$ kg (m s)$^{-1}$, and the inlet velocity v_∞ and fluid density ρ are varying parameters to simulate different fluid conditions for a given PEH. For a particular case [20], e.g., $v_\infty = 15$ m s^{-1}, $\rho = 20$ kg m^{-3}, the dynamic response of the PEH with full electrode coverage is shown in Fig. 10. The degrees of freedom of such a setup are in the order of 10^5.

4.2. Two numerical studies to validate ACC

For the above PEH, the constraint in Eq. (9) is adapted to be $0.12 \text{ m} \le x_1 < x_2 \le 0.7$ m. If x_1 and x_2 are both free parameters, the number of combinations of x_1 and x_2 required by the validation will be too large. Therefore, additional constraints are imposed on x_1, x_2, leading to the following two studies: (1) x_1 is free while $x_2 = 0.7$ m,

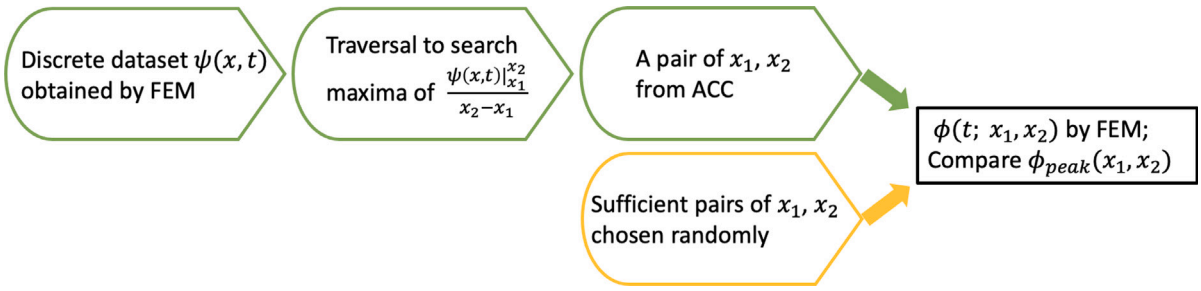

Fig. 8. Basic idea to validate ACC.

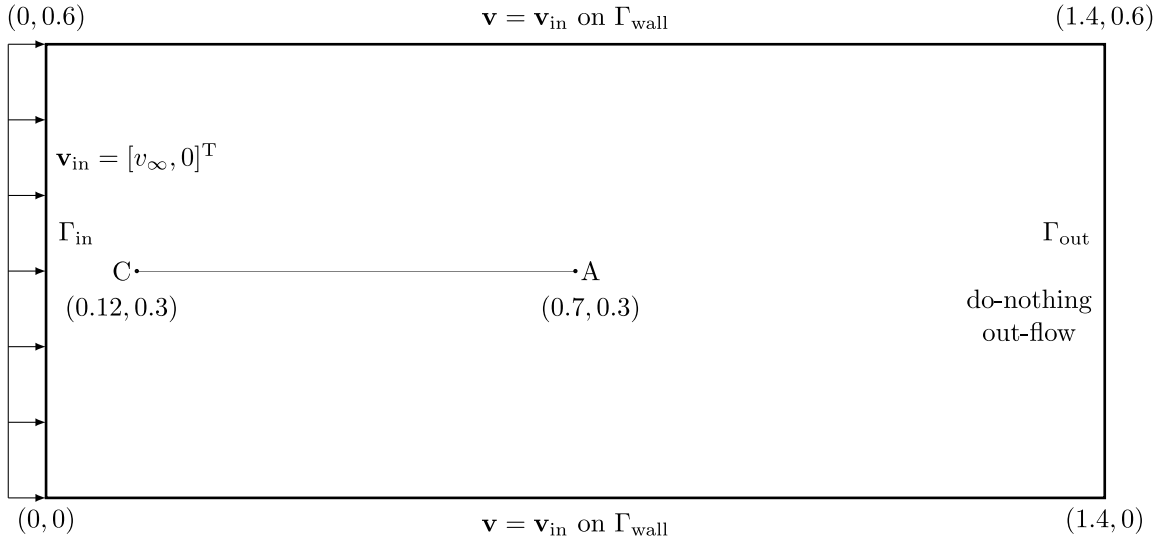

Fig. 9. Geometrical configuration and boundary conditions of the cantilevered flow-driven PEH, length unit [m].

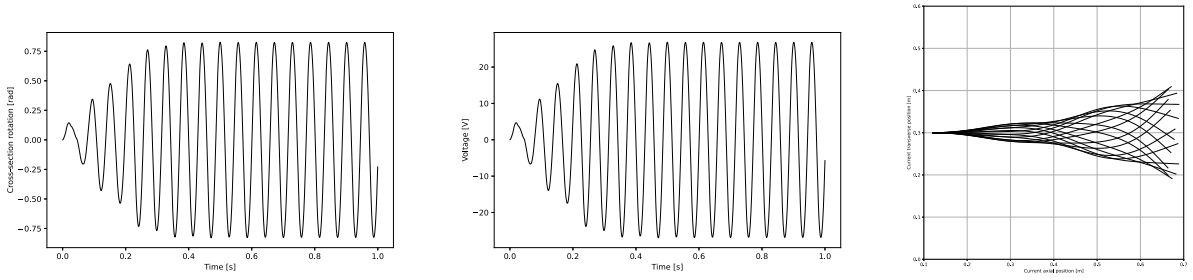

(a) Rotation at the free end (point A) (b) Voltage output (c) Deformed shapes in LCOs

(d) Pressure distribution at $t = 0.8$ s (e) Pressure distribution at $t = 0.9$ s

Fig. 10. Beam cross-section rotation, voltage output, deformation patterns and fluid pressure distribution.

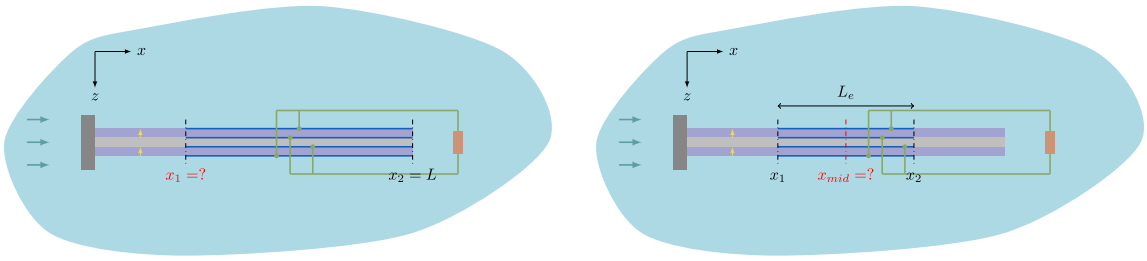

(a) Setup of numerical study one (b) Setup of numerical study two

Fig. 11. Schematic illustration of the two numerical studies.

i.e., one end of the electrode is fixed at the free tip (Point A) of the beam, but the position of the other end is unknown (Fig. 11(a)); (2) $x_2 - x_1 = 0.1$ m, i.e., the length of the electrode is fixed (0.1 m), but the position is unknown (Fig. 11(b)). For all ranges $[x_1, x_2]$, the output voltage is obtained by FEM simulations, where the electric field in the beam segment which is not covered by the electrode is assumed to be zero [22].

It is noteworthy that in the following Algorithms 1 and 2, 581 is not the number of degrees of freedom for ψ in the FEM simulation, but the number of locations where the data of ψ are collected. The reason to choose a value as large as 581 is that we aim to identify an optimal electrode configuration based on ACC, so information of ψ at sufficiently many spatial points is beneficial. On the other hand, from the perspective of temporal domain, it is obvious that the data of ψ in a single period of LCOs but not in the entire simulation time is adequate when using ACC. Hence, the time window represented by N_t time steps in Algorithms 1 and 2 only needs to cover at least one complete LCO period.

4.2.1. Numerical study one: One end of the electrode is fixed at the beam free tip

We define the percentage of electrode coverage as $\frac{x_2 - x_1}{x_A - x_C} \times 100\%$ with $x_A = 0.7$ m, $x_C = 0.12$ m. Values of x_1 are then chosen to realize 19 different percentages of $10\%, 15\%, 20\%, \ldots, 95\%, 100\%$. One exceptional value of x_1 based on ACC is found by Algorithm 1. Finally, 20 ranges of $[x_1, x_2]$ are ready for FEM simulations. Fig. 12 shows the voltage comparison of the 20 ranges under 12 different fluid conditions, where the label 'op' on the left and the red dot on the right indicate the percentage is corresponding to x_1 obtained from Algorithm 1. It is clear from the 12 sub-figures that x_1 determined by ACC is always exactly or very close to the optimal value to achieve maximum output voltage.

Algorithm 1 To find x_1 using ACC when $x_2 = 0.7$ m

Require: A list $\mathbf{x} = [0.120, 0.121, 0.122, \cdots, 0.699, 0.70]$, i.e, x coordinates of 581 points
Require: A dataset of ψ, being a $581 \times N_t$ matrix $\mathbf{Q}$, for a given fluid condition
  $\alpha \leftarrow 0$
  while $t_{ID} \in [1, 2, 3, \cdots, N_t - 1, N_t]$, $x_{ID} \in [1, 2, 3, \cdots, 579, 580]$ **do**
    $x \leftarrow$ the x_{ID}th value of list $\mathbf{x}$
    $L_e \leftarrow 0.7 - x$
    $\psi_x \leftarrow$ the element in the x_{ID}th row and the t_{ID}th column of $\mathbf{Q}$
    $\psi_{x_2} \leftarrow$ the element in the last row and the t_{ID}th column of $\mathbf{Q}$
    if $\alpha < |\psi_{x_2} - \psi_x| / L_e$ **then**
      $\alpha \leftarrow |\psi_{x_2} - \psi_x| / L_e$
      $x_1 \leftarrow x$
    end if
  end while

4.2.2. Numerical study two: Length of the electrode is fixed

In this study, $x_{mid} = (x_1 + x_2)/2$ is used to characterize different electrode coverage ranges of $[x_1, x_2]$. We choose 20 values of x_{mid}, $\{17, 20, 22, 25, 27, 30, 32, 35, 37, 40, 42, 45, 47, 50, 52, 55, 57, 60, 62, 65\} \times 0.01$ m. Two special cases: (1) $x_1 = x_C$ and (2) $x_2 = x_A$, are included. The 21st value of x_{mid} is obtained by Algorithm 2. The voltage comparison for all test cases under different fluid conditions is given by Fig. 13. The same as study one, x_{mid} computed from ACC is always exactly or very close to the optimal value to achieve maximum output voltage.

Algorithm 2 To find x_1, x_2 using ACC when $x_2 - x_1 = 0.1$ m

Require: A list $\mathbf{x} = [0.120, 0.121, 0.122, \cdots, 0.699, 0.70]$, i.e, x coordinates of 581 points
Require: A dataset of ψ, being a $581 \times N_t$ matrix $\mathbf{Q}$, for a given fluid condition
  $\alpha \leftarrow 0$
  while $t_{ID} \in [1, 2, 3, \cdots, N_t - 1, N_t]$, $x_{ID} \in [1, 2, 3, \cdots, 479, 481]$ **do**
    $x \leftarrow$ the x_{ID}th value of list $\mathbf{x}$
    $x^* \leftarrow$ the $(x_{ID} + 100)$th value of list $\mathbf{x}$
    $L_e \leftarrow x^* - x$
    $\psi_x \leftarrow$ the element in the x_{ID}th row and the t_{ID}th column of $\mathbf{Q}$
    $\psi_{x^*} \leftarrow$ the element in the $(x_{ID} + 100)$th row and the t_{ID}th column of $\mathbf{Q}$
    if $\alpha < |\psi_{x^*} - \psi_x| / L_e$ **then**
      $\alpha \leftarrow |\psi_{x^*} - \psi_x| / L_e$
      $x_1 \leftarrow x$
      $x_2 \leftarrow x^*$
    end if
  end while

4.3. Interesting relations between the voltage and the electrode length/position

The two studies above demonstrate that ACC is effective to determine an optimal range of partial electrode coverage for a fluttering PEH under different fluid conditions. For other FSI settings, e.g., vortex-induced vibration, as long as the governing equations mentioned in Sections 2.1 and 2.3 are still suitable, ACC will be also effective. What is more, some interesting phenomena can be observed from the comparison shown in Figs. 12 and 13.

(1) The output voltage of PEHs is greatly affected by their electrode configurations, underlining the importance of proper disposal of electrodes. For example, in study two (Fig. 13), although the length of the electrode is fixed, the maximum steady voltage corresponding to the optimal electrode position may be five times higher than that corresponding to a random electrode position.
(2) The maximum steady voltage does not monotonically change when the electrode length increases or the electrode moves from the clamped end to the free end. In study one (Fig. 12), the commonly used full coverage of electrode, which has the largest

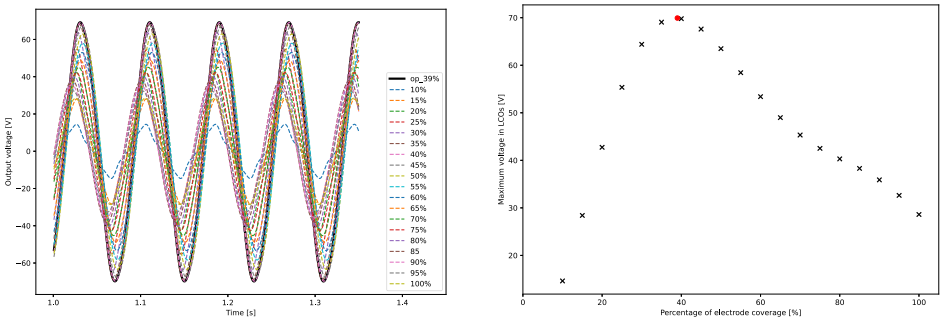

(a) $v_\infty = 10.3\ \mathrm{ms}^{-1}$, $\rho = 17.5\ \mathrm{kgm}^{-3}$

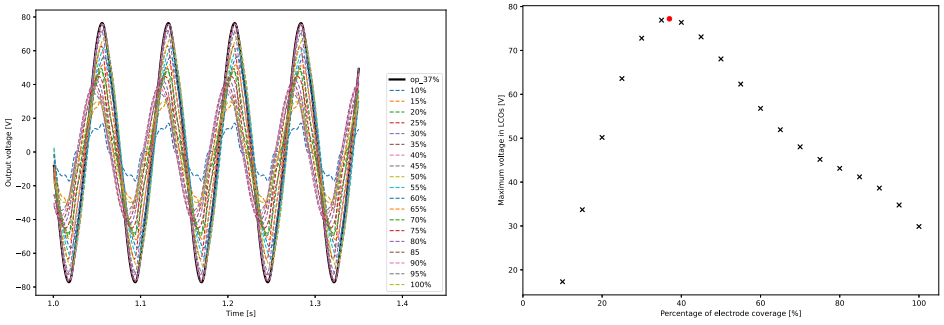

(b) $v_\infty = 10.9\ \mathrm{ms}^{-1}$, $\rho = 17.9\ \mathrm{kgm}^{-3}$

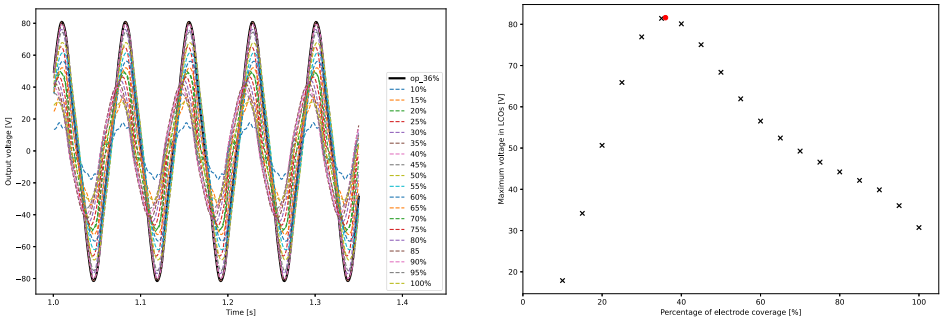

(c) $v_\infty = 11.5\ \mathrm{ms}^{-1}$, $\rho = 18.3\ \mathrm{kgm}^{-3}$

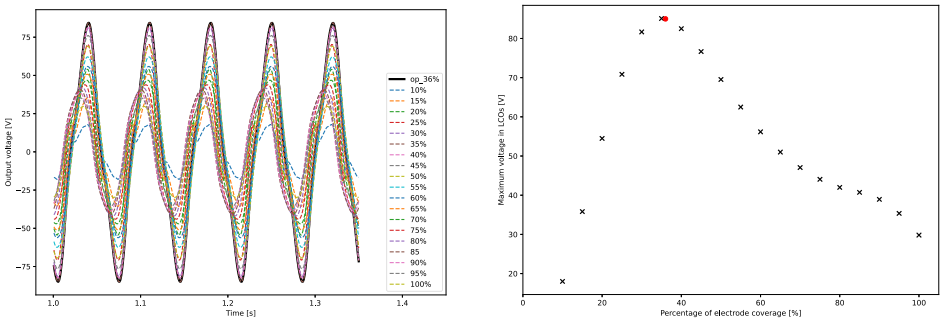

(d) $v_\infty = 12.1\ \mathrm{ms}^{-1}$, $\rho = 18.7\ \mathrm{kgm}^{-3}$

Fig. 12. Voltage in time domain (left) and maximum steady voltage (right) for different percentages of electrode coverage.

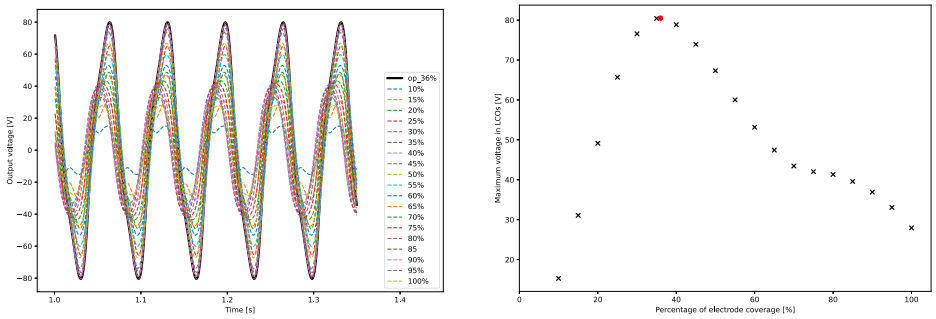

(e) $v_\infty = 12.7\ \mathrm{ms}^{-1}$, $\rho = 19.1\ \mathrm{kgm}^{-3}$

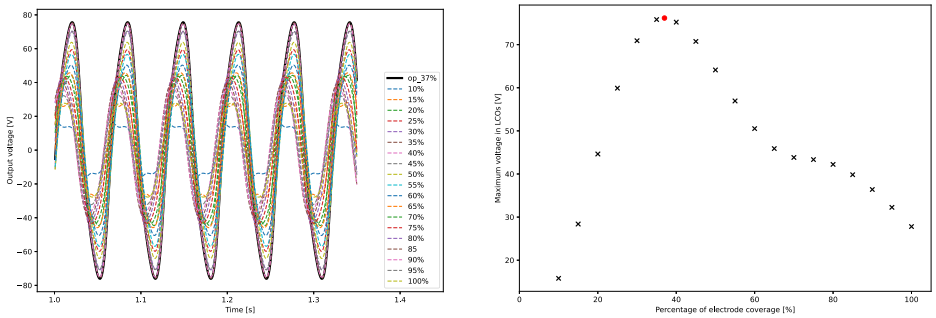

(f) $v_\infty = 13.3\ \mathrm{ms}^{-1}$, $\rho = 19.5\ \mathrm{kgm}^{-3}$

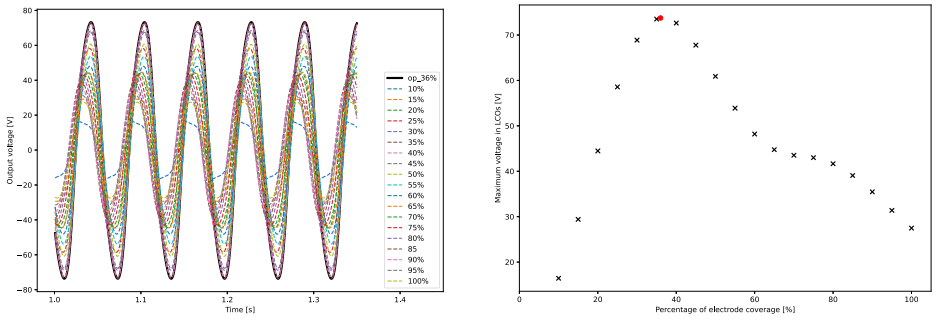

(g) $v_\infty = 13.9\ \mathrm{ms}^{-1}$, $\rho = 19.9\ \mathrm{kgm}^{-3}$

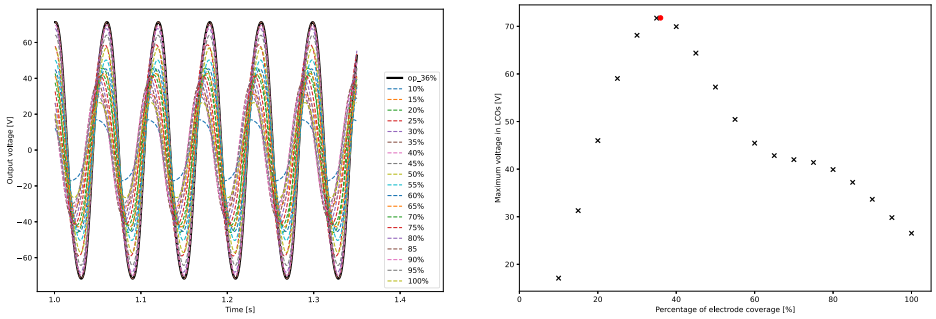

(h) $v_\infty = 14.5\ \mathrm{ms}^{-1}$, $\rho = 20.3\ \mathrm{kgm}^{-3}$

Fig. 12. (*continued*).

length, is not the worst choice of electrode configurations, but still far away from the best one. In study two (Fig. 13), the relation of the maximum steady voltage w.r.t. the electrode position is complex, with multiple local maximum and minimum values.

(3) Strain nodes obtained from modal analysis are instructive to avoid the worst design in study two (Fig. 13). For example, when $v_\infty = 10.3\ \mathrm{m\ s}^{-1}$, $\rho = 17.5\ \mathrm{kg\ m}^{-3}$, one local minimum value of the maximum steady voltage corresponds to $x_{\mathrm{mid}} = 0.2$ m, and the other one corresponds to $x_{\mathrm{mid}} = 0.4$ m. The two values indicate the first and second strain nodes in the third vibration mode of a cantilevered Euler–Bernoulli beam (Table 2), respectively, i.e., $(0.2 - 0.12)/(0.7 - 0.12) = 0.1379$, $(0.4 - 0.12)/(0.7 - 0.12) = 0.4828$. Additionally, under the first nine fluid conditions of Fig. 13, the choice of x_{mid} between 0.2 m and 0.25 m is disadvantageous. It can also be explained by strain nodes, since $x_{\mathrm{mid}} = 0.25$ m is approximately the position of the strain node in the second

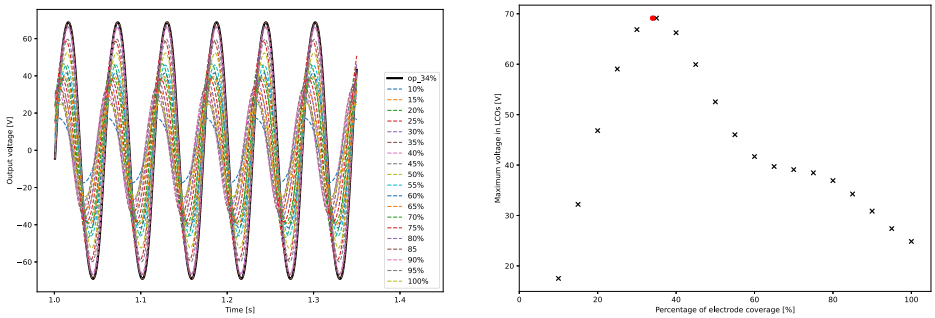

(i) $v_\infty = 15.1\ \mathrm{ms}^{-1}$, $\rho = 20.7\ \mathrm{kgm}^{-3}$

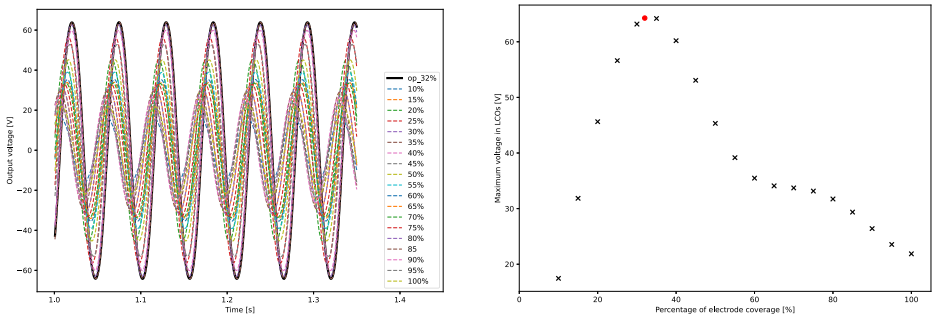

(j) $v_\infty = 15.7\ \mathrm{ms}^{-1}$, $\rho = 21.1\ \mathrm{kgm}^{-3}$

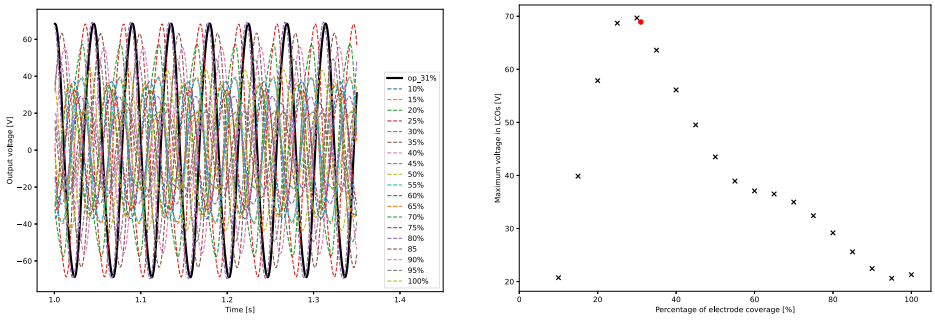

(k) $v_\infty = 16.3\ \mathrm{ms}^{-1}$, $\rho = 21.5\ \mathrm{kgm}^{-3}$

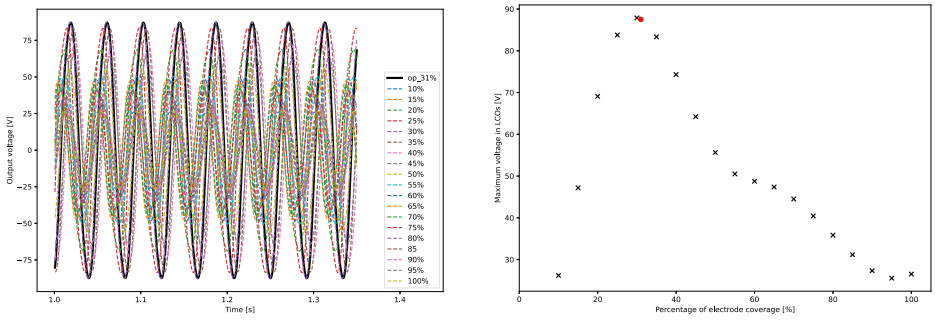

(l) $v_\infty = 16.9\ \mathrm{ms}^{-1}$, $\rho = 21.9\ \mathrm{kgm}^{-3}$

Fig. 12. (*continued*).

vibration mode. For the remaining three cases in Fig. 13, it is clear that $x_{\mathrm{mid}} = 0.17$ m is not good, because this position is close to the first strain node of the fourth and fifth vibration modes. Nevertheless, we note that strain nodes fail to provide enough information for optimal design of electrode configurations.

(4) The optimal electrode configuration is relatively stable under different fluid conditions. For study one (Fig. 12), the ideal percentage of electrode coverage from the free end drops in the range between 30% and 40%. For study two (Fig. 13), the middle point of the fixed-length electrode is favorably placed at 70%–80% of the beam length, close to the free end. The reason could be that the beam vibration patterns in LCOs do not change dramatically for the given range of fluid inlet velocity 10 m s^{-1} < v_∞ < 17 m s^{-1} and density 17 kg m^{-3} < ρ < 22 kg m^{-3}.

(5) According to the fourth phenomenon, we further conclude that in both studies, it is better to locate the electrode at the one half

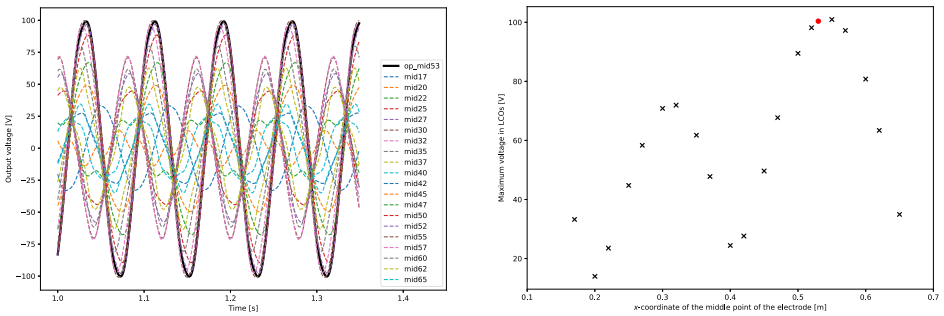

(a) $v_\infty = 10.3\ \mathrm{ms}^{-1}$, $\rho = 17.5\ \mathrm{kgm}^{-3}$

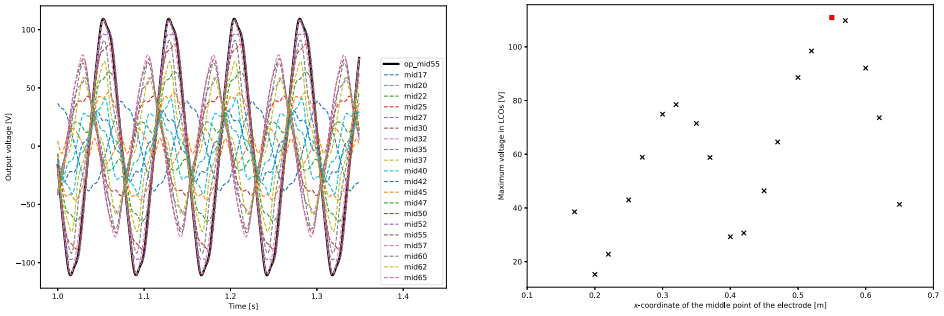

(b) $v_\infty = 10.9\ \mathrm{ms}^{-1}$, $\rho = 17.9\ \mathrm{kgm}^{-3}$

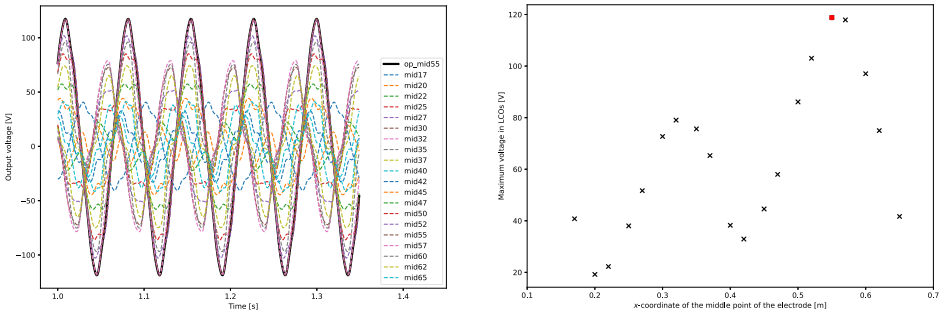

(c) $v_\infty = 11.5\ \mathrm{ms}^{-1}$, $\rho = 18.3\ \mathrm{kgm}^{-3}$

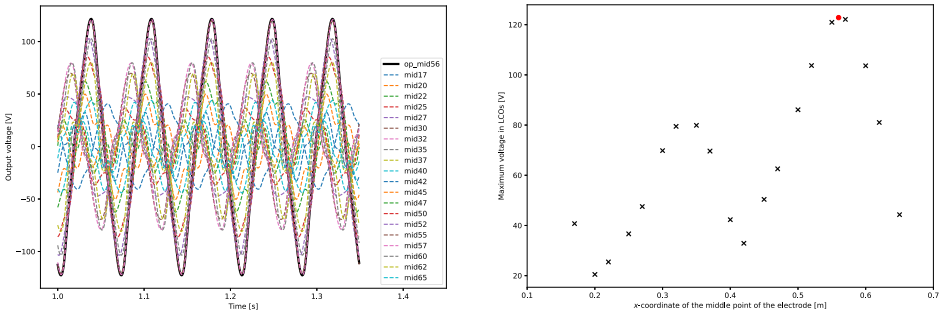

(d) $v_\infty = 12.1\ \mathrm{ms}^{-1}$, $\rho = 18.7\ \mathrm{kgm}^{-3}$

Fig. 13. Voltage in time domain (left) and maximum steady voltage (right) for different positions of electrode coverage.

length of the beam which is close to the free end, when compared with the one half close to the clamped end. The same conclusion is also drawn by paper [23]. This conclusion seems unphysical at the first glance, because the bending strain is larger at the clamped end of a cantilevered beam. However, considering that LCOs contain higher-order vibration modes, which have one or more strain nodes close to the clamped end, as seen in Table 2, it is natural that for PEHs undergoing LCOs, if the electrode length is not short enough, the one half close to the free end is a better region for electrode disposal (more likely to avoid charge cancellation).

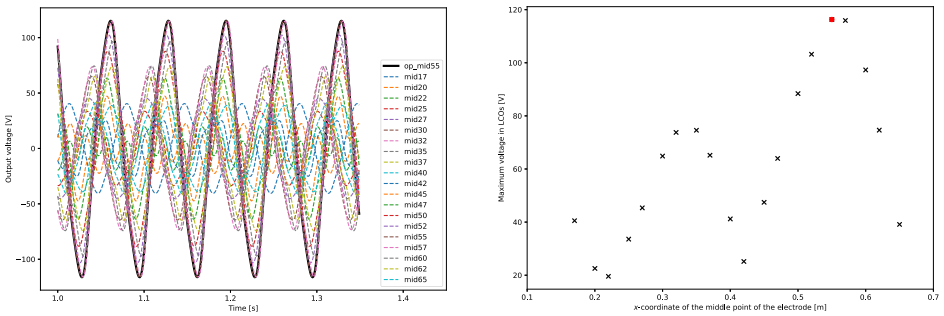

(e) $v_\infty = 12.7\ \mathrm{ms}^{-1}$, $\rho = 19.1\ \mathrm{kgm}^{-3}$

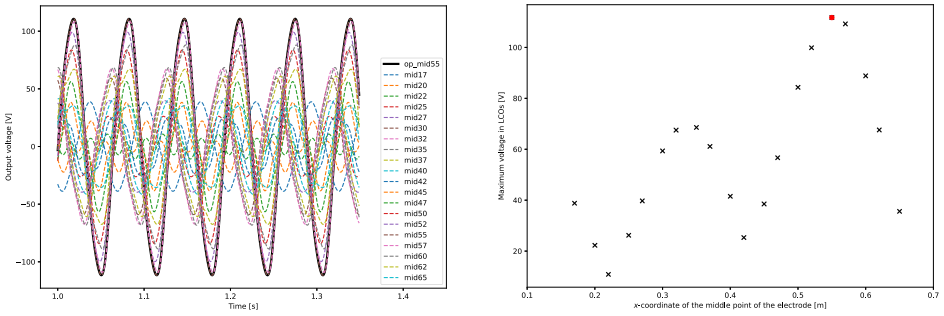

(f) $v_\infty = 13.3\ \mathrm{ms}^{-1}$, $\rho = 19.5\ \mathrm{kgm}^{-3}$

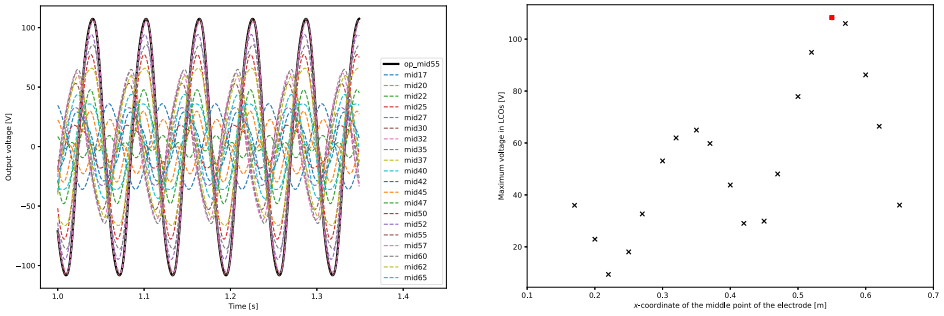

(g) $v_\infty = 13.9\ \mathrm{ms}^{-1}$, $\rho = 19.9\ \mathrm{kgm}^{-3}$

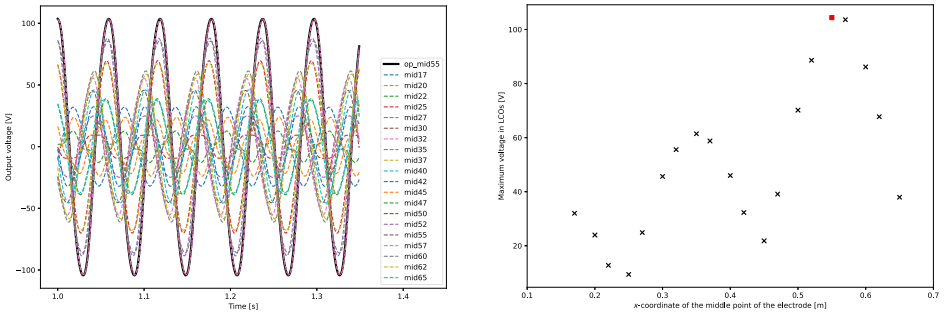

(h) $v_\infty = 14.5\ \mathrm{ms}^{-1}$, $\rho = 20.3\ \mathrm{kgm}^{-3}$

Fig. 13. (*continued*).

5. Discussions

In Section 4, considering that the number of combinations of x_1, x_2 needed by the validation will be too large if x_1 and x_2 are both free parameters, additional constraints are imposed when determining the optimal electrode configuration. Another reason for such a practice is that for the given dataset of ψ, there exists a special location where the beam curvature (i.e., $x_2 - x_1 \to 0$) is larger than any averaged curvature (i.e., $x_2 - x_1$ is a finite value), and this special location is the optimal x_{mid} found in study two. The direct inference according to ACC is that the maximum voltage output is achieved when a zero-length electrode is placed at the optimal x_{mid}, which is apparently unrealistic in physics.

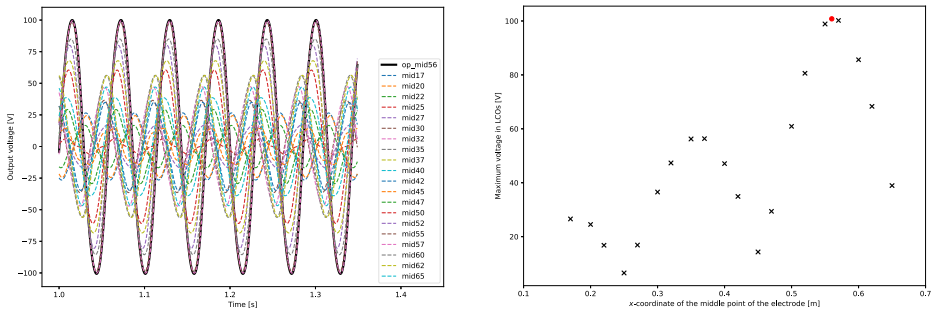

(i) $v_\infty = 15.1\ \mathrm{ms}^{-1}$, $\rho = 20.7\ \mathrm{kgm}^{-3}$

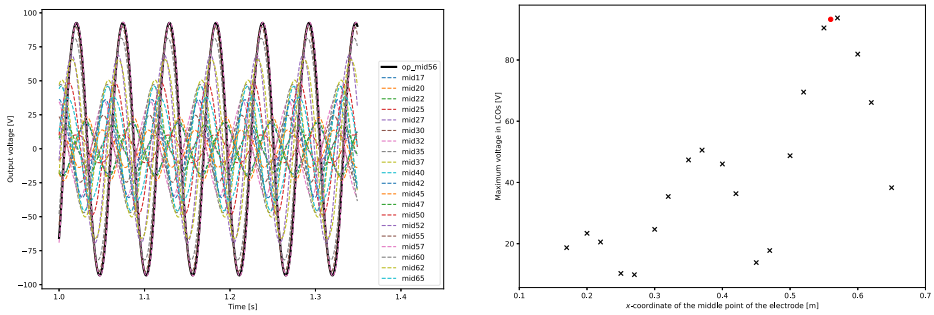

(j) $v_\infty = 15.7\ \mathrm{ms}^{-1}$, $\rho = 21.1\ \mathrm{kgm}^{-3}$

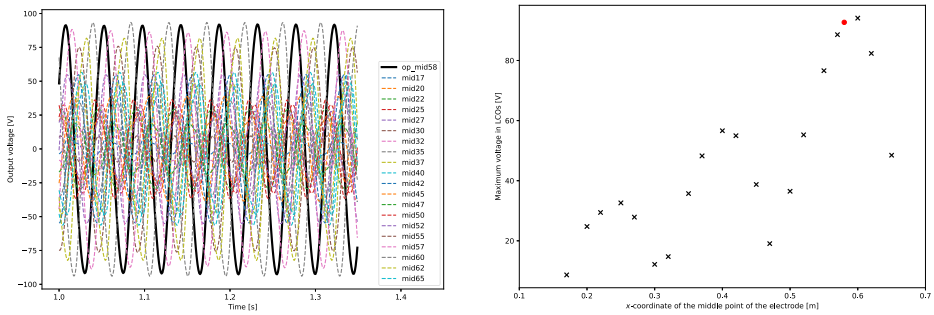

(k) $v_\infty = 16.3\ \mathrm{ms}^{-1}$, $\rho = 21.5\ \mathrm{kgm}^{-3}$

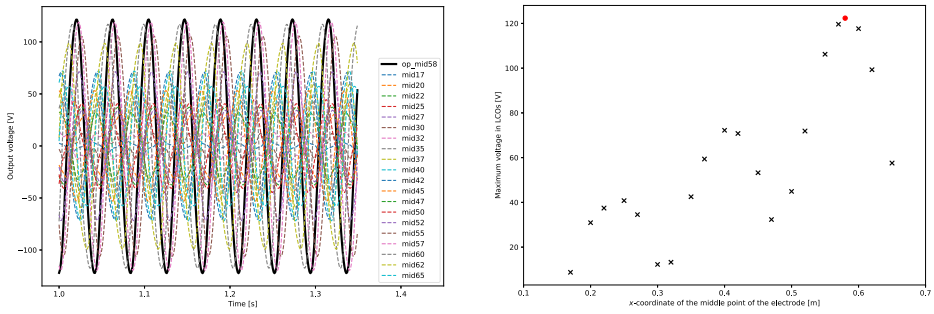

(l) $v_\infty = 16.9\ \mathrm{ms}^{-1}$, $\rho = 21.9\ \mathrm{kgm}^{-3}$

Fig. 13. (*continued*).

The reason for this unphysical result is that the intermediate indicator $\frac{\psi(x,t)|_{x_1}^{x_2}}{x_2-x_1}$ cannot always precisely track the change of the voltage output of PEHs w.r.t. x_1, x_2, due to the fact that it does not account for all terms in Eq. (8).

To explore the relation between the voltage and the electrode length, a number of FEM simulations are performed, where $x_2 - x_1$ is varying while $x_{\mathrm{mid}} = 0.55$ m (the optimal value obtained from ACC under the given fluid condition). The results of the voltage output for four values of the resistive load $R \in \{5\times10^2\ \Omega, 5\times10^3\ \Omega, 5\times10^4\ \Omega, 5\times10^5\ \Omega\}$ are shown in Fig. 14. It is clear from Fig. 14 that the higher the resistive load, the shorter the optimal electrode length is, but if the resistive load is high enough, the optimal length becomes stable, not approaching zero. It thus makes sense in physics. It also implies that ACC is more accurate when the resistive load is higher. This can be explained as follows: If going back to Eq. (8), we will find the resistive load R presents in Eq. (8-3), and Eq. (8-3) can be very small

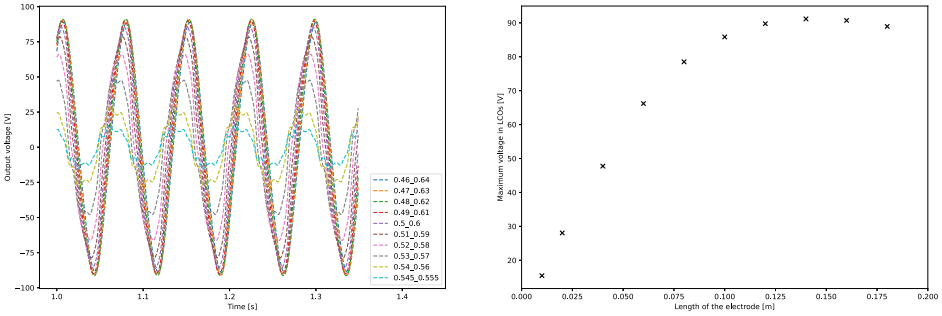

(a) Resistive load $R = 5 \times 10^2\ \Omega$

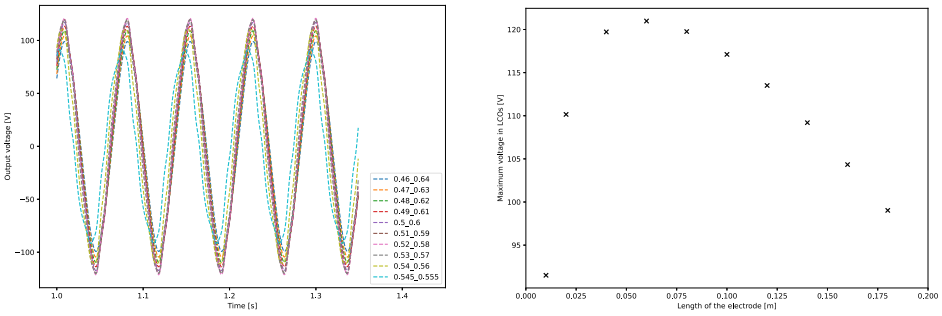

(b)Resistive load $R = 5 \times 10^3\ \Omega$

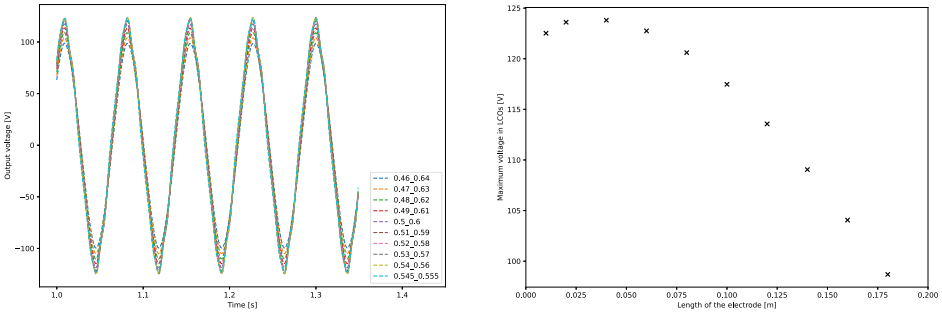

(c) Resistive load $R = 5 \times 10^4\ \Omega$

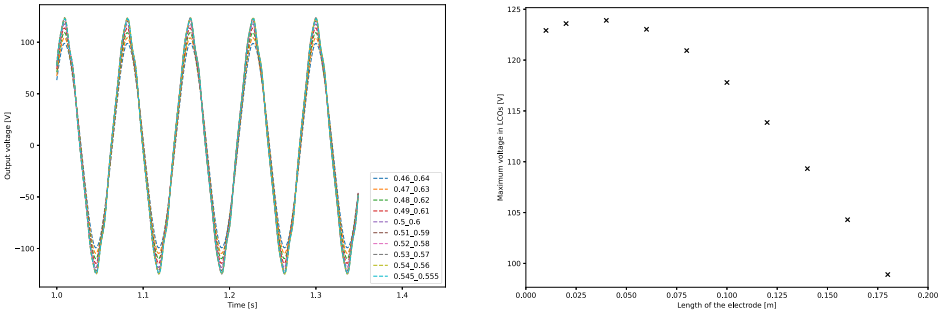

(d) Resistive load $R = 5 \times 10^5\ \Omega$

Fig. 14. Voltage in time domain (left) and maximum steady voltage (right) for different electrode length. The two numbers in each pair of the legend are the x coordinates of the two ends of the electrode. The fluid parameters are $v_\infty = 11.5$ m s^{-1} and $\rho = 18.3$ kg m^{-3}.

with an adequately large R; in such a case, the voltage mainly depends on Eq. (8-2), which happens to be the intermediate indicator of ACC with a coefficient related to the geometrical and material parameters. However, ACC being more accurate when R is higher does not mean the reason for the good results observed in the two studies of Sections 4.2.1 and 4.2.2 is that the resistive load R used in the studies is high enough. The two studies are re-performed for lower values of R, and we can still obtain the optimal electrode configuration based on ACC. This is because the intermediate indicator of ACC is actually the important multiplier shared by both Eqs. (8-2) and (8-3).

The determination of optimal parameters x_1, x_2 without imposing any additional constraints can be realized by directly maximizing the voltage expression Eq. (8). However, one issue of this approach is that it cannot provide a simple and clear rule like ACC to be easily applied in practice. Therefore, an impartial assessment for ACC could be: It

Table 2
Theoretical positions of strain nodes for a cantilevered Euler–Bernoulli beam [9].

Mode	Strain node positions on x-axis ($\bar{x} = x/L$)			
1	–	–	–	–
2	0.2165	–	–	–
3	0.1323	0.4965	–	–
4	0.0944	0.3559	0.6417	–
5	0.0735	0.2768	0.5001	0.7212

does not always work properly, but it helps to make the optimization of electrode coverage much easier.

6. Conclusions

Optimization of electrode configuration is an effective method to improve the power output of piezoelectric energy harvesters (PEHs). Most of relevant research has focused on base-excited PEHs and taken advantage of strain nodes. The present work investigates flow-driven PEHs, and proposes the averaged curvature criterion (ACC) for electrode optimization, which has superiority over strain node based methods. Firstly, the latter one only helps to avoid the bad choice of electrode configuration, while the former one indicates the good choice. Secondly, for flow-driven PEHs, e.g., PEHs undergoing flutter, the latter one is difficult to employ because there are no fixed locations of strain nodes, while no such a problem presents in the former one. ACC may fail to provide adequate instruction in some cases, but it is feasible, and increases our insights into the relation between the voltage output and the structural deformation.

ACC is derived from the analytic expression of the voltage output of a beam-like PEH as a function of the beam cross-section rotation. Experimental data for a base-excited PEH available from literature are employed to preliminarily validate ACC. It is then followed by two numerical studies of a PEH operating under limit cycle oscillations (LCOs) to validate ACC for flow-driven PEHs. The two numerical studies, one for the optimal electrode length, and the other for the optimal electrode position, are implemented under a number of fluid conditions. The results show that although the relation between the maximum steady voltage output and the electrode length or position is complex, the optimal electrode configuration does not change a lot against varying fluid conditions. For the given range of inlet velocities and fluid densities, the optimal electrode length is to cover 30%–40% of the beam from the free end, and the optimal electrode position is to place the middle point of the electrode at the 70%–80% of the beam length from the clamped end. These observations imply that for a PEH subject to LCOs, it is better to locate the electrode close to the free end of the cantilevered beam rather than the clamped end. This principle, which is unconventional since the bending strain is larger at the clamped end, is supported by the fact that LCOs contain higher-order vibration modes and their strain nodes are distributed near the clamped end, so the electrode placement close to the free end is more beneficial to avoid charge cancellation.

This work demonstrates that ACC is a simple and effective design criterion for electrode optimization to greatly improve the power output of beam-like PEHs. ACC only concerns a single pair of electrodes. Multiple pairs of electrodes with appropriate circuit connection would also enhance the power output of PEHs, and that could be one topic of our future research.

CRediT authorship contribution statement

Lan Shang: Methodology, Software, Validation, Writing – original draft. **Christophe Hoareau:** Writing – review & editing. **Andreas Zilian:** Funding acquisition, Supervision, Conceptualization, Writing – review & editing.

Declaration of competing interest

The authors declare that they have no known competing financial interests or personal relationships that could have appeared to influence the work reported in this paper.

Data availability

Data will be made available on request.

Acknowledgments

The authors gratefully acknowledge the support of the Luxembourg National Research Fund under the PRIDE programme (PRIDE17/12252781) as well as the European Union's Horizon 2020 research and innovation programme under grant agreement No 811099.

References

[1] Yang Z, Zhou S, Zu J, Inman D. High-performance piezoelectric energy harvesters and their applications. Joule 2018;2(4):642–97.
[2] Gabris MA, Ping J. Carbon nanomaterial-based nanogenerators for harvesting energy from environment. Nano Energy 2021;90:106494.
[3] Muthalif AG, Nordin ND. Optimal piezoelectric beam shape for single and broadband vibration energy harvesting: Modeling, simulation and experimental results. Mech Syst Signal Process 2015;54:417–26.
[4] Tabatabaei SMK, Behbahani S, Rajaeipour P. Multi-objective shape design optimization of piezoelectric energy harvester using artificial immune system. Microsyst Technol 2016;22(10):2435–46.
[5] Kong N, Ha DS, Erturk A, Inman DJ. Resistive impedance matching circuit for piezoelectric energy harvesting. J Intell Mater Syst Struct 2010;21(13):1293–302.
[6] Du S, Jia Y, Chen S-T, Zhao C, Sun B, Arroyo E, Seshia AA. A new electrode design method in piezoelectric vibration energy harvesters to maximize output power. Sensors Actuators A 2017;263:693–701.
[7] Fu H, Chen G, Bai N. Electrode coverage optimization for piezoelectric energy harvesting from tip excitation. Sensors 2018;18(3):804.
[8] Arnau A, Soares D. Fundamentals of piezoelectricity. In: Piezoelectric transducers and applications. Springer; 2009, p. 1–38.
[9] Erturk A, Tarazaga PA, Farmer JR, Inman DJ. Effect of strain nodes and electrode configuration on piezoelectric energy harvesting from cantilevered beams. J Vib Acoust 2009;131(1).
[10] Stewart M, Weaver PM, Cain M. Charge redistribution in piezoelectric energy harvesters. Appl Phys Lett 2012;100(7):073901.
[11] Hu K, Zhou B, Wang F, Yang Z, Wang M. Influence of effective electrode coverage on the energy harvesting performance of piezoelectric cantilevers. Energy Convers Manage 2021;248:114758.
[12] Krishnasamy M, Qian F, Zuo L, Lenka T. Distributed parameter modeling to prevent charge cancellation for discrete thickness piezoelectric energy harvester. Solid-State Electron 2018;141:74–83.
[13] Kashyap R, Lenka T, Baishya S. A model for doubly clamped piezoelectric energy harvesters with segmented electrodes. IEEE Electron Device Lett 2015;36(12):1369–72.
[14] De Marqui Jr C, Tan D, Erturk A. On the electrode segmentation for piezoelectric energy harvesting from nonlinear limit cycle oscillations in axial flow. J Fluids Struct 2018;82:492–504.
[15] Tang L, Païdoussis MP, Jiang J. The dynamics of variants of two-dimensional cantilevered flexible plates in axial flow. J Sound Vib 2009;323(1–2):214–31.
[16] Reissner E. On one-dimensional finite-strain beam theory: the plane problem. Z Angew Math Phys ZAMP 1972;23(5):795–804.
[17] Shang L, Hoareau C, Zilian A. A geometrically nonlinear shear deformable beam model for piezoelectric energy harvesters. Acta Mech 2021;232(12):4847–66.
[18] Erturk A, Inman DJ. An experimentally validated bimorph cantilever model for piezoelectric energy harvesting from base excitations. Smart Mater Struct 2009;18(2):025009.
[19] Dietl J, Wickenheiser A, Garcia E. A Timoshenko beam model for cantilevered piezoelectric energy harvesters. Smart Mater Struct 2010;19(5):055018.
[20] Shang L, Hoareau C, Zilian A. Modeling and simulation of thin-walled piezoelectric energy harvesters immersed in flow using monolithic fluid–structure interaction. Finite Elem Anal Des 2022;206:103761.
[21] Tang L, Païdoussis MP, Jiang J. Cantilevered flexible plates in axial flow: energy transfer and the concept of flutter-mill. J Sound Vib 2009;326(1–2):263–76.
[22] Wang H, Tang L, Shan X, Xie T, Yang Y. Modeling and performance evaluation of a piezoelectric energy harvester with segmented electrodes. Smart Struct Syst 2014;14(2):247–66.
[23] Piñeirua M, Doaré O, Michelin S. Influence and optimization of the electrodes position in a piezoelectric energy harvesting flag. J Sound Vib 2015;346:200–15.